

# Magnetic Interactions and Cluster Formation: Boosting Surface Thermopower in Topological Insulators

M. Tirgar,<sup>1</sup> H. Barati Abgarmi,<sup>1</sup> and J. Abouie<sup>1,\*</sup>

<sup>1</sup>*Department of Physics, Institute for Advanced Studies in Basic Sciences (IASBS), Zanjan 45137-66731, Iran*

This study theoretically investigates the thermoelectric properties of magnetic topological insulators (TIs), with a focus on the effects of magnetic atom exchange interactions on the thermopower of their surfaces. Our findings demonstrate that interactions among magnetic atoms significantly enhance the Seebeck coefficient. The formation of magnetic clusters through exchange interactions increases the scattering of Dirac electrons, thereby improving the thermoelectric power factor. We conducted extensive Monte Carlo simulations across various configurations, including ferromagnetic and antiferromagnetic bulk materials, comparing magnetic clustering in Ising and Heisenberg models. Special attention was given to cluster definitions related to surface critical temperatures. Our analysis indicates that the size and number of magnetic clusters influence relaxation times, as well as electrical and thermal resistivities, ultimately affecting the thermopower. Optimized interlayer and intralayer interactions can elevate the surface thermopower of TIs to values comparable to those observed in antiferromagnetic MnTe, renowned for its unique spin-based thermoelectric properties. This work highlights the potential of magnetic TIs for thermoelectric applications and sets the stage for future research.

## I. INTRODUCTION

Achieving net-zero greenhouse gas emissions is crucial in our lives today, and developing systems capable of generating clean energy is a vital task across various research fields[1]. Thermoelectric generators, which convert waste heat into clean energy, are as efficient as other renewable energy sources like solar cells[2]. The pursuit of high-performance thermoelectric materials has garnered significant attention due to their potential applications in technology[3]. The primary challenge in developing these materials lies in the strong interdependence of the thermopower factor, electrical conductivity, and thermal conductivity. Typically, increasing electrical conductivity decreases thermopower and increases thermal conductivity. Therefore, strategies for developing new thermoelectric materials should focus on mitigating this interdependence, requiring innovative approaches and the use of materials with unique properties[4].

While thermoelectric coefficients are generally interdependent in conventional materials, magnetic materials with spin-driven thermoelectrics can significantly alter this relationship. For instance, in anisotropic layered magnetic systems such as antiferromagnetic MnTe, thermopower displays anomalous enhancement in the disordered paramagnetic phase above the Neel temperature[5]. In this system, the paramagnon-electron drag thermopower has emerged as a compelling phenomenon, exhibiting continuous enhancement in the paramagnetic phase and offering the potential for high-performance thermoelectric devices[6–8].

Topological systems are also excellent thermoelectric materials, exhibiting strong spin-orbit coupling crucial for spin-driven thermoelectrics[9, 10]. Topological in-

ulators (TIs) exhibit insulating behavior in their bulk while possessing conductive surface states [11]. Surface electrons with a Dirac-like spectrum are resistant to perturbations that preserve the system's time-reversal symmetry. When doped with magnetic atoms, these surface states develop an energy gap, leading to exotic phenomena such as the anomalous Hall effect [12] and giant anisotropic magnetoresistance[13, 14]. In TIs lightly doped with magnetic atoms, the anisotropic relaxation time of surface electrons results in anisotropic magnetoresistance. In magnetic TIs such as the van der Waals TI MnBi<sub>2</sub>Te<sub>4</sub>, interactions of magnetic atoms and the sequential scattering of surface electrons significantly influence transport properties. These magnetic atoms form temperature-dependent clusters on the surface, affecting the material's magnetic, electric, and thermoelectric characteristics[15, 16].

In this paper, we investigate the thermoelectric properties of the surface of intrinsic magnetic topological insulators (TIs) by examining the effects of exchange interactions among magnetic atoms. On the surface of magnetic TIs, these atoms typically reside on a triangular lattice and interact with their neighbors via an exchange spin Hamiltonian, leading to the formation of magnetic clusters. The formation of these clusters through exchange interactions increases the scattering of Dirac electrons, thereby boosting thermoelectric efficiency. The clusters are randomly distributed across the surface of the TIs and act as scattering centers, influencing surface transport properties.

We apply the semiclassical Boltzmann formalism to calculate relaxation times, electrical and thermal resistivities, and the thermopower factor as functions of the mean size and number of clusters. Extensive Monte Carlo (MC) simulations [17] are performed to obtain the temperature dependence of the mean size and number of clusters. We compare magnetic clustering on the surface of TIs where the exchange interaction between mag-

---

\*Electronic address: jahana@iasbs.ac.ir

netic atoms is modeled by Ising and Heisenberg models, focusing on cluster definitions relative to surface critical temperatures. Our simulations encompass various configurations, including ferromagnetic and antiferromagnetic bulk phases.

Our analysis reveals that the size and number of magnetic clusters significantly affect relaxation times, electrical and thermal resistivities, and the thermopower factor. We demonstrate that optimized interlayer and intralayer interactions can elevate the surface thermopower of TIs to around  $170 \mu\text{V}/\text{K}$ , which is comparable to that of  $\text{Bi}_2\text{Te}_3$  and its alloys, thereby underscoring the potential of magnetic TIs for advanced thermoelectric applications. This value is also comparable to that of antiferromagnetic  $\text{MnTe}$ , a material used in spin-based thermoelectrics, where paramagnon drag causes an anomalous increase in thermopower above the Neel temperature, with thermopower values ranging from 100 to 200  $\mu\text{V}/\text{K}$  for pure  $\text{MnTe}$  to Li-doped  $\text{MnTe}$ .

Additionally, we show that predictions of thermopower using Mott's relation become less reliable above the critical temperature due to the linear energy dependence of surface states. Furthermore, the Wiedemann-Franz law holds only at low temperatures, with deviations at higher temperatures resulting from spin-orbit interactions and the presence of magnetic clusters. This work highlights the promise of magnetic TIs for thermoelectric applications and paves the way for future research.

## II. EXCHANGE INTERACTIONS AND MAGNETIC CLUSTERING ON THE SURFACE OF MAGNETIC TIS

Before exploring the magnetic properties of magnetic TIs, we briefly review their typical lattice structure. Intrinsic magnetic TIs, whether antiferromagnetic such as the chalcogenide semiconductors  $\text{MnBi}_2\text{Te}_4$  and  $\text{MnBi}_4\text{Te}_7$ , or ferromagnetic like  $\text{MnBi}_6\text{Te}_{10}$  are composed of  $\text{Bi}_2\text{Te}_3$  and  $\text{MnTe}$  substances. The former features a layered structure formed by the stacking of septuple (Te-Bi-Te-Mn-Te-Bi-Te) triangular layers[18], while the latter compounds consist of  $\text{MnBi}_2\text{Te}_4$  units bridged by one or two  $\text{Bi}_2\text{Te}_3$  layers (see Fig. 1).

All atoms in the outermost septuple layer, which separates the TI from its environment, contribute to the surface properties. The magnetic atoms in this layer interact with surface Dirac electrons, thereby influencing the surface transport properties.

Inelastic neutron scattering experiments on  $\text{MnBi}_2\text{Te}_4$  single crystals have demonstrated that the exchange interactions between Mn atoms are well-described by the Heisenberg spin Hamiltonian with uniaxial single-ion anisotropy [19, 20]. These measurements also reveal significant interlayer exchange interactions and substantial lifetime broadening.

The exchange interactions between Mn atoms with spin  $\tilde{s} = 5/2$  are described by the following exchange

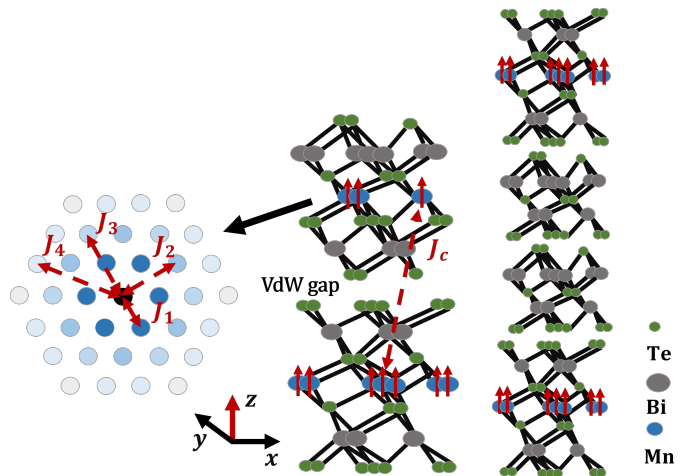


FIG. 1: Left: A triangular lattice of Mn atoms, with exchange constants  $J_1$  to  $J_4$  representing interactions from nearest-neighbor to fourth-neighbor. In  $\text{MnBi}_2\text{Te}_4$ , they are characterized by the parameters  $\tilde{s}J_1 \approx 0.30$ ,  $\tilde{s}J_2 \approx -0.083$ ,  $\tilde{s}J_3 \approx 0$ , and  $\tilde{s}J_4 \approx 0.023$  millielectron-Volt (meV), as reported in Ref. [19]. Middle: the lattice structure of the antiferromagnetic  $\text{MnBi}_2\text{Te}_4$ , which consists of two septuple layers separated by a van der Waals gap, with  $J_c$  representing the interlayer interaction between magnetic atoms. Right: the lattice structure of the ferromagnetic TI  $\text{MnBi}_6\text{Te}_{10}$ , in which two  $\text{Bi}_2\text{Te}_3$  layers are placed between two  $\text{MnBi}_2\text{Te}_4$  layers.

Hamiltonian [19]:

$$H = - \sum_{\langle i,j \rangle_{\parallel}} J_{ij} \tilde{s}_i \cdot \tilde{s}_j - J_c \sum_{\langle i,j \rangle_{\perp}} \tilde{s}_i \cdot \tilde{s}_j - D \sum_i (\tilde{s}_i^z)^2. \quad (1)$$

This Hamiltonian is derived from fitting neutron scattering data to a local-moment Heisenberg model, limited to fourth-nearest neighbors within layers of Mn atoms. The first sum accounts for intra-triangular-layer interactions from nearest-neighbor to fourth-nearest neighbors, the second sum covers interlayer nearest-neighbor interactions, and the final term represents the uniaxial single-ion anisotropy. The uniaxial anisotropy is in the  $z$ -direction, normal to the surface of the magnetic TI (see the figure 1). This anisotropy significantly influences the transport properties of the TI, making the relaxation time isotropic and thereby eliminating anisotropic magnetoresistance.

Numerous experiments [21–24], particularly those investigating giant magnetoresistance (GMR) phenomena [22], have demonstrated that spins orientation in magnetic materials significantly influences their electrical resistivity. In particular, they reveal that the resistivity increases in the paramagnetic phase where the spins are randomly oriented. This behavior is attributed to the formation of magnetic clusters, whose size and number are temperature-dependent. In the following sections, we demonstrate that magnetic clustering on the surface of magnetic TIs, significantly influences the transport properties of the system. We define magnetic clusters within the Ising and Heisenberg models separately, and deter-

mine their size and number's temperature dependence using Monte Carlo (MC) simulations.

### A. Magnetic clustering on the surface of TIs: Ising Hamiltonian

Before delving into the original system, we consider the interaction of magnetic atoms on the surface of magnetic TIs to be described by a classical Ising Hamiltonian:  $H = -J_1 \tilde{s}^2 \sum_{\langle i,j \rangle} n_i n_j$ , where  $J_1 > 0$  is the ferromagnetic exchange constant, and  $n_i$  denotes the classical spin at the  $i$ th lattice site, taking values of  $\pm 1$ . Given the Ising-like anisotropy in magnetic TIs, our findings in this context can offer valuable insights into the original system.

The two-dimensional Ising model on a triangular lattice with ferromagnetic exchange interaction exhibits two distinct phases [25]. At low temperatures, the system resides in a ferromagnetic phase characterized by non-zero magnetization. As temperature increases, thermal fluctuations disrupt the long-range order. At a critical temperature  $k_B T_c \approx 4.2 J_1 \tilde{s}^2$ , the magnetic order is destroyed, transitioning the system to a paramagnetic phase. In the ferromagnetic phase, magnetic clusters are formed by spins antialigned with the lattice magnetization. In the paramagnetic phase, although the magnetization is zero and long-range order is absent, domains with short-range order can exist at lower temperatures. Clustering in this phase occurs based on maximum exchange energy, with spins possessing the highest energy forming clusters.

Using MC simulations, we computed the size and number of clusters at various temperatures. To achieve equilibrium at a given temperature  $T$ , we used the final configuration from the last MC step at a lower temperature  $T' = T - \delta T$ . To ensure thermal equilibrium, we performed  $10^5$  MC steps per spin, followed by statistical averaging over an additional  $10^5$  MC steps per spin. Our results for the number of clusters and their mean size are presented in Fig. 2. As shown, for both ferromagnetic ( $J_c > 0$ ) and antiferromagnetic ( $J_c < 0$ ) interlayer exchange couplings,  $\xi$  and  $n_c$  are small at low temperatures, increase with rising temperature, peak at the critical temperature  $T_c$ , and then decrease with further increases in temperature.

### B. Magnetic clustering on the surface of TIs: Heisenberg Hamiltonian

In this section, we consider the exchange interaction of magnetic atoms on the surface of the TI to be described by the Heisenberg model in Eq. (1). It has been demonstrated that this model on a triangular lattice exhibits various long-range orders. In a triangular spin lattice with ferromagnetic exchange interactions between nearest-neighbor spins ( $J_1 > 0$ ) and antifer-

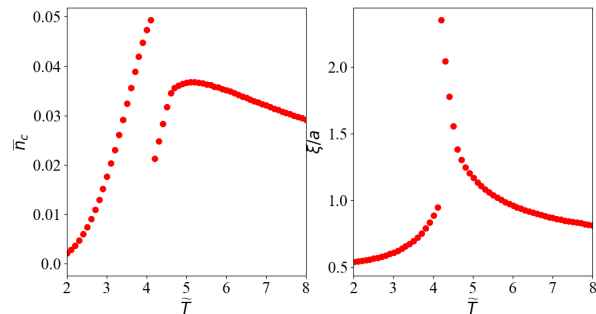


FIG. 2: The MC results (Ising Hamiltonian) for the number of magnetic clusters per unit area,  $\bar{n}_c$  (left), and the size of magnetic clusters,  $\xi/a$  (right), as functions of temperature,  $\tilde{T} = k_B T / (J_1 \tilde{s}^2)$ . Here,  $k_B$  denotes the Boltzmann constant,  $\tilde{s}$  represents the spin of the magnetic atoms,  $J_1$  is the nearest-neighbor exchange interaction, and  $a$  is the triangular lattice constant. The interaction of magnetic atoms on the surface of the magnetic TI is described by the Ising Hamiltonian. The number and size of clusters behave independently of the type of interlayer interaction, be it antiferromagnetic ( $J_c < 0$ ) or ferromagnetic ( $J_c > 0$ ). Here, the interlayer interaction  $|J_c|$  is scaled to  $J_1$ , and set to 0.24 [19]. The critical temperature is about  $\tilde{T}_c \simeq 4.2$  for both  $J_c < 0$  and  $J_c > 0$  cases.

romagnetic exchange interactions between next-nearest-neighbor spins ( $J_2 < 0$ ), the ground state is ferromagnetic when  $J_2 \ll J_1$ . However, it transitions to an incommensurate short-range ordered phase at  $|J_2/J_1| = 1/3$  [26].

In most magnetic materials with magnetic ions arranged in a triangular lattice, such as  $\text{LiNiO}_2$  [26], the ratio of coupling constants  $J_2/J_1 < 1/3$  results in a ferromagnetic ground state. However, at non-zero temperatures, thermal fluctuations disrupt this magnetic order, leading to a paramagnetic phase at all temperatures, as predicted by the Mermin-Wagner theorem.

In intrinsic antiferromagnetic TIs like  $\text{MnBi}_2\text{Te}_4$  and  $\text{MnBi}_4\text{Te}_7$ , uniaxial single-ion anisotropy breaks the  $\text{SU}(2)$  symmetry, thereby allowing the surface of the TI to maintain ferromagnetic order even at finite temperatures. However, as the temperature increases, thermal fluctuations become more significant, eventually causing a transition to a paramagnetic phase at a critical temperature  $T_c$ . Additional interactions, such as ferromagnetic interactions with the fourth neighbors, further stabilize the ferromagnetic order within the triangular layer.

When the interaction of magnetic atoms on the surface of the TI is described by the Heisenberg model, the lattice spins can adopt various orientations. At zero temperature, due to easy-axis anisotropy, they are completely aligned along the  $z$ -direction, with the magnetization per spin being  $m^z = \tilde{s}$ , where  $\tilde{s}$  is the spin value of magnetic atoms. As the temperature increases, some spins (referred to as defect spins) orient opposite to the magnetization, forming magnetic clusters.

A spin can be a member of a cluster if it meets the

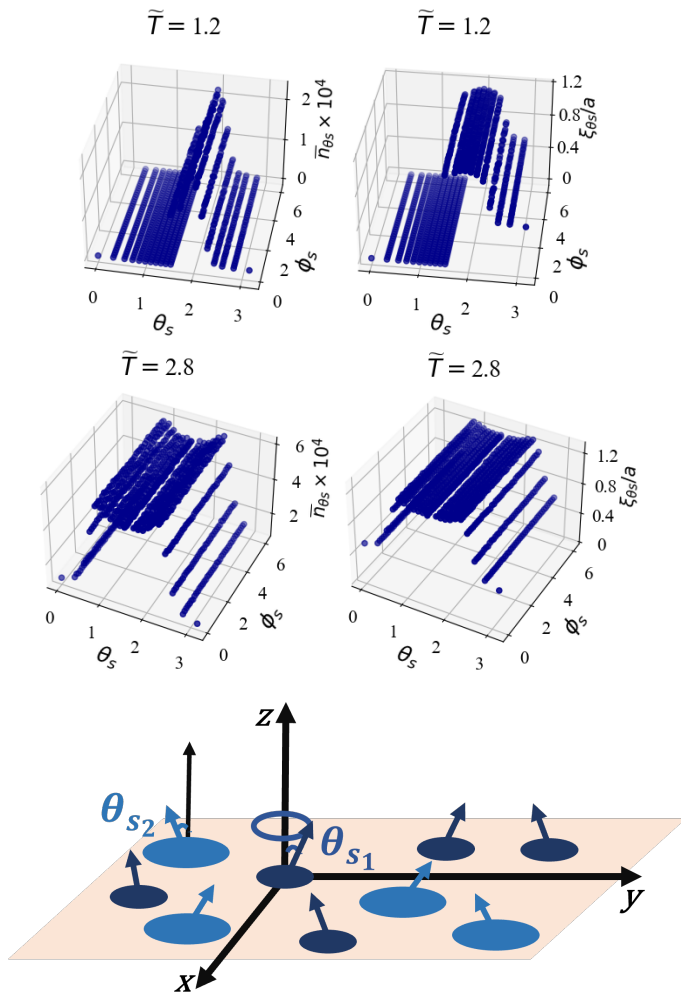


FIG. 3: The MC results (Heisenberg Hamiltonian) for the size and number of clusters of different types, for two distinct temperatures below ( $\bar{T} = 1.2$ ) and above ( $\bar{T} = 2.8$ ) the critical temperature ( $\bar{T}_c = 1.42$ ). Here,  $\bar{T} = k_B T / (J_1 \bar{s}^2)$ , with  $J_1$  being the nearest-neighbor exchange constant. For each  $\theta_s$ , they are independent of  $\phi_s$ . The schematic illustration of cluster formation on the surface of a magnetic TI (bottom). When the interaction of magnetic atoms is described by the Heisenberg Hamiltonian, various types of clusters form, characterized by their  $s_z$  or spin angles  $\theta_s$  (see also the actual MC simulation results presented in Fig. 4). Here, we schematically depict two types of clusters, distinguished by their spin angles  $\theta_{s_1}$  and  $\theta_{s_2}$ . The spin of clusters of the same type are oriented such that their in-plane components cancel each other out on average.

following conditions: (1) its  $z$ -component is opposite to the lattice magnetization, and (2) it is a nearest neighbor to a spin in the cluster. Once these criteria are met, the spin becomes a cluster member with the Wolff probability  $P = 1 - \exp(-2E/k_B T)$  [27, 28], where  $E$  refers to the energy of links connecting the spins to their first to fourth-nearest neighbors.

Our MC simulations show that the clusters formed on

the surface of the TI have different  $s^z$  values. Therefore, we classify the clusters based on their  $s^z$  values or their angle  $\theta_s$  relative to the  $z$ -axis, treating them as independent defects that scatter electrons independently. Furthermore, our MC simulations indicate that the symmetric nature of the Heisenberg interaction, combined with an on-site anisotropy term  $D(\tilde{s}^z)^2$ , results in clusters where the spins are oriented such that their in-plane components cancel each other out on average. Specifically, as illustrated schematically in Fig. 3, for a cluster oriented at an angle  $(\theta_s, \phi_s)$ , there exists a corresponding cluster at an angle  $(\theta_s, -\phi_s)$ . Consequently, these clusters have on average a single spin component in the  $z$ -direction, quantified as  $s_{\theta_s} = s \cos \theta_s$ , with  $s$  being the spin of clusters.

To determine the size and number of clusters in the Heisenberg model, we performed the following steps:

1. At a specified temperature  $T$ , allow the system to reach equilibrium.
2. Randomly select a spin and identify the cluster it belongs to.
3. Add neighboring spins to the cluster using the Wolff probability. Below the critical temperature, the magnetization of the surface is nonzero, and the spins that are not aligned with the magnetization form clusters.
4. Replace the spins in the cluster with their average spin.
5. Repeat steps 3 and 4 for the newly added spins.
6. Repeat steps 2 to 5 until all spins have been visited.
7. Record the average number and size of clusters [29], along with the direction indicated by the angles  $\theta_s$  and  $\phi_s$ , for analytical calculations.
8. Increase the temperature by  $\delta T$  and use the final state from the previous temperature as the initial state.
9. Repeat steps 1 to 8 for the desired temperature range.

Unlike the Ising model, where the clustering mechanism differs in the ferromagnetic and paramagnetic phases, the Heisenberg model applies the same steps in the paramagnetic phase. In this phase, short-range ordered regions lead to a larger scattering amplitude compared to the ferromagnetic phase. Since neighboring spins with the same orientation exhibit a higher Wolff probability, this probability is also used to construct magnetic clusters in the paramagnetic regime.

We have also plotted in Fig. 5 the size and number of clusters of different types as a function of temperature. At temperatures below the critical temperature, only clusters with negative  $s_z$ , depicted in red, appear

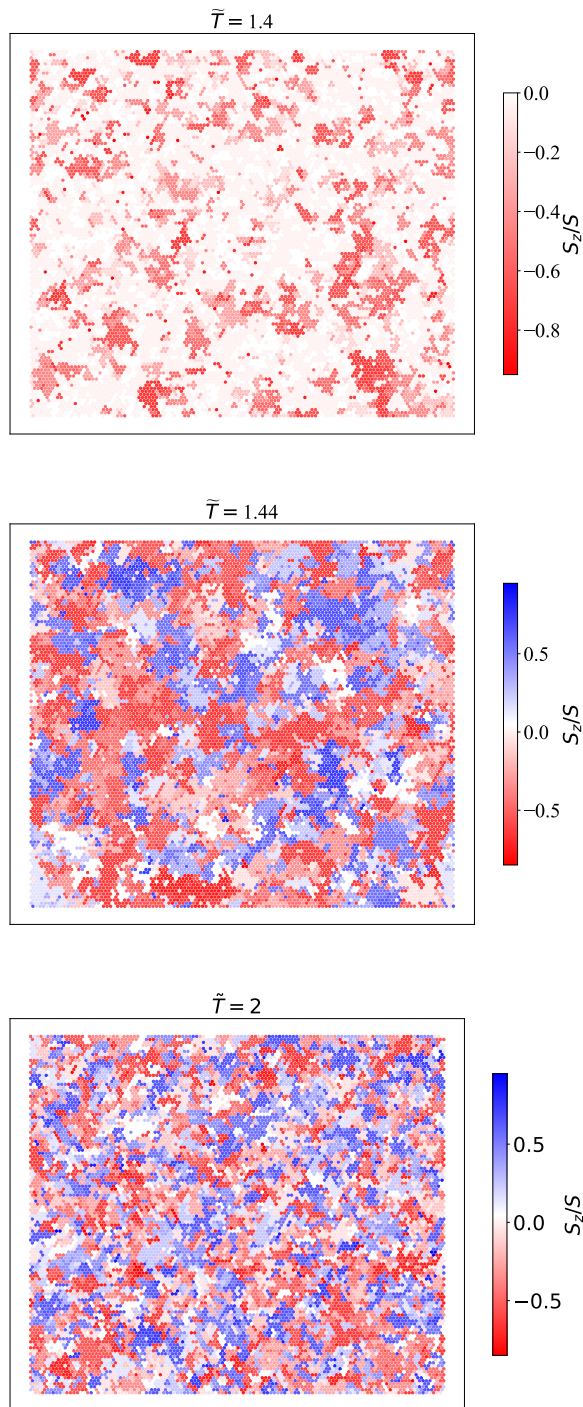


FIG. 4: Monte Carlo results for the real shapes of various magnetic clusters characterized by the ratio  $s_z/s$ , formed on the surface of a topological insulator due to the Heisenberg interaction among magnetic atoms, at different temperatures  $\tilde{T} = k_B T / (J_1 \tilde{s}^2)$ . Here, the exchange interactions between magnetic atoms are governed by the Heisenberg spin Hamiltonian in Eq. (1). Here,  $J_1$  is the nearest-neighbor exchange coupling, and the exchange couplings  $J_2$  and  $J_4$ , the uniaxial single-ion anisotropy  $D$ , and the interlayer exchange  $J_c$  are scaled to  $J_1$  with values set to  $-0.28$ ,  $0.08$ ,  $0.4$ , and  $-0.18$ , respectively. Different colors denote various cluster types. In the ordered phase, below the critical temperature  $\tilde{T}_c = 1.42$ , all clusters exhibit a negative spin value  $s_z < 0$  (surface magnetization is along the  $+z$ -direction). As the system crosses the critical point, clusters with  $s_z > 0$  emerge on the surface. Above the critical point, increasing temperature results in smaller cluster sizes.

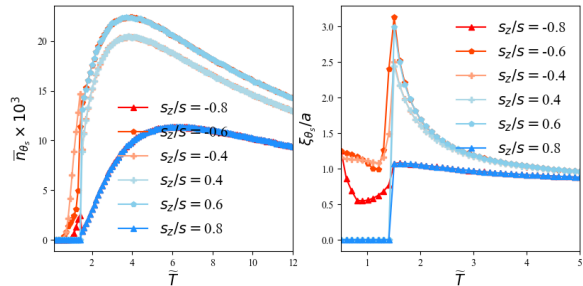


FIG. 5: The number and size of magnetic clusters of different types, labeled by  $s_z/s = \cos \theta_s$ , as functions of temperature. The interaction of magnetic atoms on the surface of the magnetic TI is described by the Heisenberg Hamiltonian. The interlayer interactions are antiferromagnetic ( $J_c < 0$ ), with  $|J_c|/J_1 = 0.18$ . At temperatures below the critical temperature, only clusters with negative  $s_z$ , depicted in red, appear on the surface of the TI, while above the critical temperature, all types of clusters emerge.

on the surface of the TI, while above the critical temperature, all types of clusters emerge.

In the antiferromagnetic phase, magnetic clusters exhibit comparable numbers and sizes for spins with equal magnitudes of  $|s_z|$ . In fact, there is no notable difference between the magnetic clusters characterized by  $|s_z|$  and those characterized by  $-|s_z|$ .

We performed our MC simulations initially for a finite number of stacked layers, each containing magnetic ions on a triangular lattice in the  $xy$ -plane. We considered a two-dimensional lattice with  $120 \times 120$  sites under periodic boundary conditions. To enhance computational efficiency and improve system simulation, we initially focused on a limited number of layers.

To investigate the impact of the number of layers, we systematically increased the number of layers and compared the results to a system with periodic boundary conditions along the  $z$ -axis. Our simulations show that when the number of layers is about ten, the magnetization behavior converges to that of a periodic system in the  $z$ -direction (see Fig. 6). This indicates that a ten-layer magnetic TI exhibits behaviors akin to those of 3D magnetic TIs, supporting previous research [30, 31].

### III. SCATTERING POTENTIAL AND RELAXATION TIME

The dynamics of Dirac electrons on the surface of magnetic TIs is described by the Bloch Hamiltonian:

$$H_{\vec{k}} = \hbar v_F (\vec{k} \times \vec{\sigma}) \cdot \hat{z} + J_b M \sigma_z. \quad (2)$$

Here, the unit vector  $\hat{z}$  is considered normal to the surface of the TI, the Fermi velocity is denoted by  $v_F$ , and the momentum of Dirac electrons is given by  $\vec{k} = k_x \hat{x} + k_y \hat{y}$ . The vector of Pauli matrices,  $\vec{\sigma}$ , represents the spin of

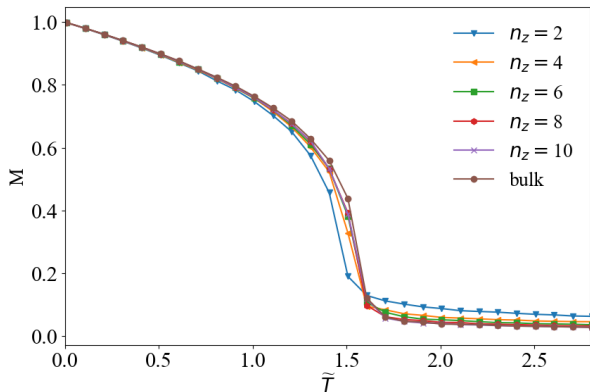


FIG. 6: The bulk magnetization per spin as a function of temperature for various numbers of layers ( $n_z$ ). Here, the intralayer interaction is given by the Heisenberg model with nearest-neighbor exchange interaction  $J_1$ , and the interlayer interaction is set of  $J_c/J_1 = -0.18$ . This result shows that a TI with  $n_z = 10$  magnetic layers can fully reflect the magnetic properties of the 3D TI.

Dirac electrons. The magnetization  $M$ , arising from bulk magnetic atoms, introduces an energy gap of  $2J_b M$  to the surface energy spectrum. Here,  $J_b$  represents an effective exchange interaction between surface electrons and the magnetic atoms within the bulk. This energy gap leads to phenomena such as skew scattering and the anomalous Hall effect. The magnetization  $M$  is temperature-dependent. At temperatures higher than the critical temperature of the bulk  $T > T_c^{\text{bulk}}$ , the magnetization is zero, resulting in gap-closing in the system. Therefore, when examining the thermoelectric properties of the magnetic TI, this temperature dependence should be considered in our formalism. The energy spectra and wavefunctions of the Dirac electrons are given by:

$$\epsilon_k = \pm \sqrt{(\hbar v_F k)^2 + J_b^2 M^2}, \quad (3)$$

and  $\psi_k(\vec{r}) = \frac{1}{\sqrt{A}} e^{i\vec{k}\cdot\vec{r}} |u_{k\pm}\rangle$ , with:

$$|u_{k+}\rangle = \begin{pmatrix} -ie^{-i\phi_k} \cos \frac{\eta_k}{2} \\ \sin \frac{\eta_k}{2} \end{pmatrix}, |u_{k-}\rangle = \begin{pmatrix} ie^{-i\phi_k} \sin \frac{\eta_k}{2} \\ \cos \frac{\eta_k}{2} \end{pmatrix}, \quad (4)$$

where  $k = |\vec{k}| = (k_x^2 + k_y^2)^{1/2}$ ,  $\cos \eta_k = J_b M / |\epsilon_k|$  and  $\phi_k = \tan^{-1}(k_y/k_x)$ .

As discussed in the previous section, exchange interactions between magnetic atoms lead to magnetic clustering on the surface of the TI. These clusters are randomly distributed, uncorrelated, and scatter electrons, resulting in surface magnetoresistance. To determine the scattering rate, we express the scattering potential in terms of the clusters' mean size  $\xi$  as follows [15, 17]:

$$H_{\sigma s} = J_0 \exp\left(-|\vec{r} - \vec{R}|/\xi\right) \vec{\sigma}_{\vec{r}} \cdot \vec{s}_{\vec{R}}, \quad (5)$$

where  $\vec{s}$  is the spin of the cluster, and  $J_0$  is the exchange coupling between the Dirac electron at  $\vec{r}$  and the cluster at  $\vec{R}$ .

Expressing the scattering potential in terms of the clusters' mean size allows us to examine the effects of temperature and phase transitions on the surface's transport properties.

In electron scattering from a magnetic impurity, both the spin and size of the magnetic impurity are typically considered in the scattering potential. This includes an  $s-d$  term and a Dirac delta term for charge scattering. However, in the scattering potential described in Eq. (5), both terms are already incorporated.

When the interaction between magnetic atoms on the surface of the TI is described by the Ising Hamiltonian, the spins  $\vec{s}$  of the clusters are perpendicular to the TI's surface. In this scenario, the scattering rate is isotropic and depends solely on  $\Delta\vec{k} = \vec{k} - \vec{k}'$ . The relaxation time can be derived from:

$$\frac{1}{\tau_k} = A \int \frac{d^2 k'}{2\pi^2} w(\vec{k}, \vec{k}') (1 - \cos \Delta\phi), \quad (6)$$

where  $w(\vec{k}, \vec{k}')$  is the transition rate between the two eigenstates  $|\vec{k}\rangle$  and  $|\vec{k}'\rangle$  of the Hamiltonian (2), and  $\Delta\phi = \phi_k - \phi_{k'}$ . Using Fermi golden rule the transition rate simply reads:

$$w(\vec{k}, \vec{k}') = \frac{2\pi}{\hbar} n_c |T_{\vec{k}, \vec{k}'}|^2 \delta(\epsilon_k - \epsilon_{k'}), \quad (7)$$

where  $n_c$  is clusters number. In various systems,  $J_0$  typically amounts to one or two orders of magnitude less than the Fermi energy. For magnetic topological insulators (TIs),  $J_0$  is on the order of 10 meV (for example, in  $\text{MnBi}_2\text{Te}_4$ ,  $J_0 \sim 25$  meV[33]), reflecting a weak scattering potential that justifies the use of the first Born approximation. Within this approximation, the  $T$ -matrix is obtained as follows:

$$T_{\vec{k}, \vec{k}'} = J_0 s \sum_{\vec{r}, \vec{R}} \langle \vec{k} | \exp\left(-|\vec{r} - \vec{R}|/\xi\right) \int d^2 r |\vec{r}\rangle \langle \vec{r} | \vec{k}' \rangle. \quad (8)$$

The relaxation time is therefore calculated as:

$$\frac{1}{\tau_k} = \frac{1}{\tau_0} \bar{n}_c k \xi (\xi/a)^3 \frac{3 + (1 + 4k^2 \xi^2) \cos^2 \eta_k}{\sin \eta_k (1 + 4k^2 \xi^2)^{5/2}}, \quad (9)$$

where  $\tau_0 = \frac{\sqrt{3}\hbar^2 v_F}{2\pi^2 J_0^2 s^2 a}$  is a constant with the dimension of time, and  $\bar{n}_c = n_c/N$  represents the average number of clusters per triangular lattice site ( $N$ ). The constant  $\sqrt{3}a^2/2$  is the area occupied by each magnetic atoms positioned on a triangular lattice. In the case of square lattice this constant reduces to  $a^2$ .

The situation differs when the interaction of magnetic atoms on the surface of the TI is described by the Heisenberg Hamiltonian in Eq. (1). In this case, as discussed previously, various types of clusters form on the TI surface, each identified by its spin angle relative to the  $z$ -axis ( $\theta_s$ ). These clusters act as different types of defects,

scattering electrons independently. The relaxation time of Dirac electrons scattering off clusters with spin angle  $\theta_s$  is given by:

$$\frac{1}{\tau_{k,\theta_s}} = \frac{1}{\tau_0} \bar{n}_{\theta_s} k \xi_{\theta_s} \left( \frac{\xi_{\theta_s}}{a} \right)^3 \frac{g(\theta_s, \eta_k)}{\sin \eta_k (1 + 4k^2 \xi_{\theta_s}^2)^{5/2}}, \quad (10)$$

where  $g(\theta_s, \eta_k) = \cos^2 \theta_s [3 + (1 + 4k^2 \xi_{\theta_s}^2) \cos^2 \eta_k] + 2(1 + k^2 \xi_{\theta_s}^2) \sin^2 \eta_k \sin^2 \theta_s$ . Here,  $\xi_{\theta_s}$  is the mean size of clusters with spin angle  $\theta_s$ , and  $\bar{n}_{\theta_s}$  is their number per unit area.

The total relaxation time of Dirac electrons is obtained using Matthiessen's rule as:

$$\frac{1}{\tau_k} = \sum_{\theta_s} \frac{1}{\tau_{k,\theta_s}}. \quad (11)$$

The relaxation times in both the Ising and Heisenberg models depend on temperature through the temperature dependence of the cluster size and number, as well as the surface gap ( $2M$ ). In layered compounds such as  $\text{MnBi}_2\text{Te}_4$  and  $\text{MnBi}_4\text{Te}_7$ , the interlayer interactions are antiferromagnetic[32], and the bulk has A-type Neel order resulting in vanishing bulk magnetization and gapless surface states. Conversely, in compounds like  $\text{MnBi}_6\text{Te}_{10}$ , ferromagnetic interlayer interactions magnetize the bulk[32], leading to a gap in the surface states. Unlike the cluster size and number, which increase with rising temperature, the surface gap decreases due to the reduction in bulk magnetization. At the bulk critical point the magnetization becomes zero, causing the surface gap to close ( $\cos \eta_k = 0$ ). For temperatures above  $T_c^{\text{bulk}}$ , the gap remains closed, and the temperature dependence of the relaxation times is primarily influenced by the behavior of the cluster size and number.

Figure 7 illustrates the relaxation time of gapless Dirac electrons ( $M = 0$ ) as a function of temperature, for the parameters  $J_0 = 25 \text{ meV}$ [33],  $s = 5/2$ ,  $v_F = 5.5 \times 10^5 \text{ m/s}$ ,  $a = 4.33 \text{ \AA}$ , and  $\tau_0 \simeq 1.3 \times 10^{-14} \text{ s}$ . The relaxation behaviors are similar in both the Ising and Heisenberg models. At low temperatures, the cluster size and number are small, resulting in a low scattering amplitude and consequently a long relaxation time. As the temperature increases, the relaxation time decreases rapidly due to the growth in cluster size and number. At the surface critical temperature, the cluster size and number reach their maximum, leading to the minimum relaxation time. Above the critical temperature, in the disordered phase, the relaxation time increases smoothly.

#### IV. THERMOELECTRIC PROPERTIES

At a given temperature  $T$ , the efficiency of thermoelectric materials is characterized by the figure of merit  $zT = \frac{S^2 \sigma}{\kappa} T$ , where  $\sigma$ ,  $S$ , and  $\kappa$  represent electrical conductivity, thermoelectric power factor (thermopower), and thermal conductivity, respectively. These properties

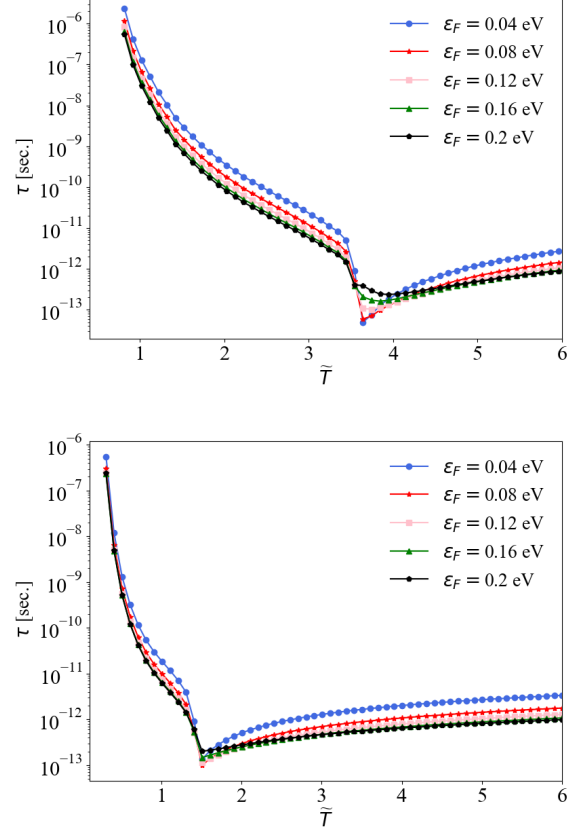


FIG. 7: The temperature-dependent relaxation time of Dirac electrons, for various Fermi energies, under the influence of magnetic clusters on the surface of magnetic TIs. The interactions are modeled using the Ising (up) and Heisenberg (down) Hamiltonians. In the Heisenberg case,  $J_1$  represents the nearest-neighbor exchange coupling, while  $J_2$ ,  $J_4$ , the uniaxial single ion anisotropy  $D$ , and the interlayer exchange  $J_c$  are scaled to  $J_1$ , with values set to  $-0.28$ ,  $0.08$ ,  $0.4$ , and  $-0.18$ , respectively.

vary with temperature due to the temperature dependence of the relaxation time  $\tau_k$ . They are expressed in terms of  $\tau_k$  as:

$$\gamma^{(i)}(T) = \int \frac{e^{2-i}}{4\pi} \tau_k (\epsilon_k - \mu)^i v_k^2 \left( \frac{-\partial f^0}{\partial \epsilon_k} \right) k dk, \quad (12)$$

where  $e$  is the electron charge,  $v_k$  is band velocity,  $\mu$  is the chemical potential, and  $f^0$  is Fermi-Dirac distribution function. The functions  $\gamma^{(i)}$  with  $i = 0, 1$ , and  $2$  correspond to  $\gamma^{(0)} = \sigma$ ,  $\gamma^{(1)} = \sigma S T$ , and  $\gamma^{(2)} = \kappa T$ . The temperature dependence of the chemical potential  $\mu$  is as:

$$\mu(T) = \epsilon_F \left[ 1 - \frac{\pi^2}{3} \left( \frac{k_B T}{\epsilon_F} \right)^2 \right]^{1/2}, \quad (13)$$

where  $\epsilon_F$  is the Fermi energy. As the surface density of states is linear with surface energy, i.e.  $g(\epsilon) =$

$\epsilon/(2\pi\hbar^2v_F^2)$ , the above expression for the chemical potential is exact.

At sufficiently low temperatures, the chemical potential approximates the Fermi energy,  $\mu \simeq \epsilon_F$ , allowing the derivative of the Fermi-Dirac distribution function to be approximated by the Dirac delta function,  $\delta(\epsilon_k - \epsilon_F)$ . In this regime, the electrical conductivity is given by  $\sigma = c\tau_{k_F}$ , where  $c$  is a constant, while both the thermal conductivity and the thermopower vanish. As temperature increases, the chemical potential decreases according to Eq. (13), reaching zero at  $k_B T \simeq \epsilon_F/2$ . For Fermi energies ranging from 10 to 200 meV, the corresponding temperatures range from 100 K to 2000 K, some of which are significantly higher than the stability temperature of magnetic TIs. The van der Waals interactions in magnetic TIs ensure the stability of their crystal structure up to approximately 500 – 600 K; however, beyond this temperature, these interactions diminish in significance, leading to a transition of the crystal into flakes [34, 35].

Various proposals have been made to maintain material stability at high temperatures, one of which involves applying external pressure [36, 37]. It has been demonstrated that applying pressure can raise the stability temperature to 900 K. Therefore, our subsequent investigations into the effects of high temperatures are justified.

### A. Ising case: Antiferromagnetic interlayer interactions

When the interaction between magnetic atoms on the surface of magnetic TIs is described by the Ising model, the relaxation time of Dirac electrons is given by Eq. (9). For intrinsic antiferromagnetic TIs like  $\text{MnBi}_2\text{Te}_4$ , the bulk exhibits Neel order with a finite staggered magnetization below the Neel temperature  $T_N = 25$  K, transitioning to a paramagnetic phase above  $T_N$ . In both phases, the magnetization  $M$  is zero, resulting in a vanishing surface gap. Consequently, in this scenario,  $\cos \eta_k = 0$ , and the relaxation time simplifies to:

$$\frac{1}{\tau_k} = \frac{1}{\tau_0} \bar{n}_c k \xi (\xi/a)^3 \frac{3}{(1 + 4k^2 \xi^2)^{5/2}}. \quad (14)$$

As a result, the electrical and thermal resistivities can be determined by numerically solving the integrals presented in Eq. (12).

Figure 8 presents the plots of surface electrical and thermal resistivities as functions of rescaled temperature  $\tilde{T} = k_B T / (J_1 \tilde{s}^2)$ . Both resistivities exhibit similar behavior: At temperatures significantly below the surface critical temperature ( $\tilde{T} < 4.2$ ), they remain low and nearly independent of the Fermi energy. As the temperature rises, the resistivities increase gradually. Near the critical temperature, they escalate sharply due to the influence of magnetic clustering on the surface of the TI. Around this critical temperature, the dependence on the

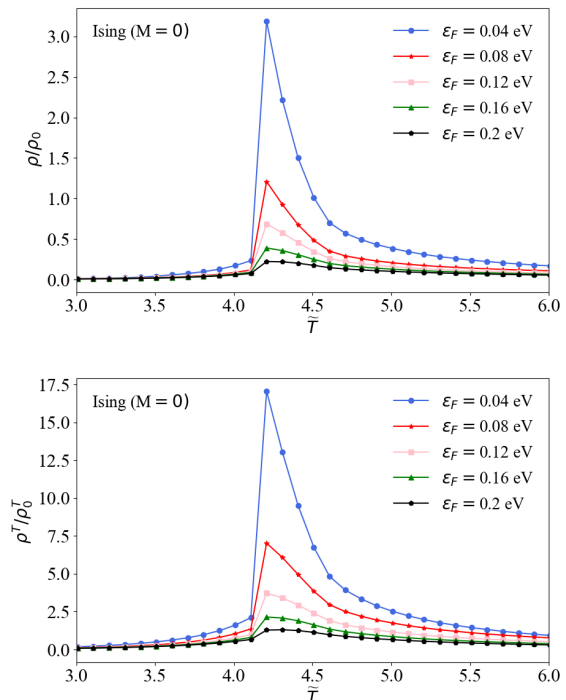


FIG. 8: Transport properties of the surface of antiferromagnetic TIs as functions of temperature for various Fermi energies, considering the interaction between magnetic atoms on the surface of the TI described by the Ising Hamiltonian with nearest neighbor exchange interaction  $J_1$ . The plots show: electrical resistivity (up) and thermal resistivity (down). Here, the interlayer interaction  $J_c$  is scaled to  $J_1$ , and set to  $-0.18$ . The parameters  $\rho_0$  and  $\rho_0^T$  are defined as follows:  $\rho_0 = \frac{4\pi^2 J_0^2 s^2 a^2}{\sqrt{3} \hbar^2 v_F^2} \frac{\hbar}{c^2}$ ,  $\rho_0^T = \frac{8\pi^3 J_0^2 s^2 a^3}{\sqrt{3} \hbar^2 v_F^3 k_B}$ . Both  $\rho_0$  and  $\rho_0^T$  are constants with dimensions of electrical resistivity and thermal resistivity, respectively. For magnetic TIs, with parameters  $J_0 = 25$  meV,  $v_F = 5.5 \times 10^5$  m/s,  $a = 4.33$  Å, and  $s = \frac{5}{2}$ , these constants are estimated to be  $3250 \Omega$  and  $4.5 \times 10^7$  K/W, respectively.

Fermi energy becomes more pronounced. Above the critical temperature, in the paramagnetic phase, the resistivities decrease with increasing temperature, which are attributed to the behavior of magnetic clusters. At high temperatures, magnetic clusters shrink to the size of individual spins, and their number decreases, leading to a reduction in resistivity.

In Figure 9, the thermopower is plotted as a function of temperature. The maximum thermopower observed within the studied temperature range is approximately  $170 \mu\text{V}/\text{K}$ , which is comparable to  $\text{Bi}_2\text{Te}_3$  and its alloys. In bismuth telluride alloys, this high thermopower is attributed to the widening of the energy gap and the suppression of intrinsic conduction effects [38]. Conversely, in magnetic TIs, significant thermopower is primarily due to magnetic clustering on the surface. This value is also comparable to that of antiferromagnetic  $\text{MnTe}$ , a

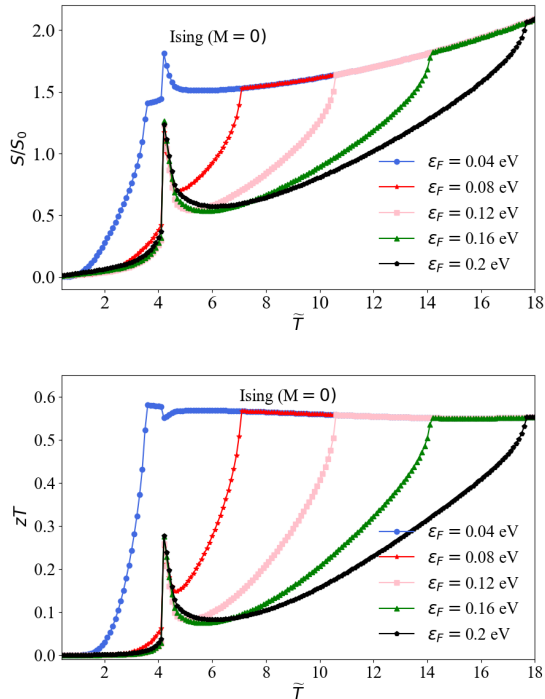


FIG. 9: Thermoelectric properties of the surface of magnetic TIs as functions of temperature for various Fermi energies. The interaction between magnetic atoms on the TI surface is modeled using the Ising Hamiltonian with nearest neighbor exchange interaction  $J_1$ . The plots illustrate the thermopower (up) and the thermoelectric figure of merit (down), with the interlayer interaction  $J_c$  is scaled to  $J_1$ , and set to  $-0.18$ . The thermopower is scaled to  $S_0 = \frac{k_B}{e} \simeq 86.17 \mu\text{V}/\text{K}$ .

material used in spin-based thermoelectrics. In MnTe, paramagnon-drag causes an anomalous increase in thermopower above the Neel temperature ( $T_N \simeq 305$  K), with thermopower values ranging from 100 to 200  $\mu\text{V}/\text{K}$  for pure MnTe to Li-doped MnTe [5].

Across various Fermi energy values, two distinct and noticeable changes are observed in the behavior of both the thermopower and the thermoelectric figure of merit. At low temperatures, the thermopower and figure of merit are minimal due to the absence of magnetic clusters on the surface. As the temperature increases, magnetic clusters form, leading to a significant increase in thermopower. Near the surface critical temperature  $\tilde{T}_c \simeq 4.2$  ( $T_c \simeq 70$  K), the thermopower abruptly jumps and reaches a maximum at the critical point. For higher Fermi energy values, this maximum is approximately  $S \simeq S_0 = 86.17 \mu\text{V}/\text{K}$ , while for lower Fermi energy values, this maximum reaches  $S \simeq 1.8S_0 = 155 \mu\text{V}/\text{K}$ .

Above the critical temperature, in the paramagnetic phase, magnetic clusters reduce in size, and eventually reaching the size of individual spins at very high temperatures. In this phase, when the Fermi energy exceeds  $2k_B T_c$ , the thermopower initially declines but subsequently rises, changing its behavior at the tempera-

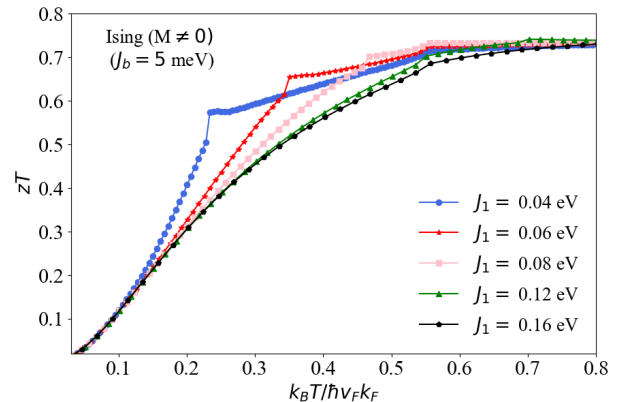


FIG. 10: Thermoelectric figure of merit as a function of  $k_B T / \hbar v_F k_F$  for various nearest-neighbor exchange coupling  $J_1$ . The interaction between magnetic atoms on the surface of the TI is governed by the Ising Hamiltonian. Here,  $J_1$  represents the nearest-neighbor exchange coupling, and the antiferromagnetic interlayer exchange  $J_c$  is scaled to  $J_1$ , and set to  $-0.18$ .

ture where the chemical potential vanishes. Despite the shrinking of magnetic clusters, the thermopower continues to rise as the chemical potential decreases with increasing temperature, as in Eq. (13). The anomaly in the thermopower curve manifests at  $k_B T \approx \varepsilon_F/2$ . For  $\varepsilon_F < 2k_B T_c$ , this anomaly is seen below the critical temperature, while for higher Fermi energies, it is seen above the critical temperature.

It should be emphasized that the observed behavior of the thermopower is primarily due to magnetic clustering. Notably, the increase in the thermopower at high temperatures is absent without interactions between magnetic atoms, underscoring the crucial role of magnetic clustering.

The thermopower anomaly is observed at temperatures ranging from 460 K to 2300 K, corresponding to Fermi energy values between 40 meV and 200 meV. The van der Waals materials such as  $\text{MnBi}_2\text{Te}_4$  remain stable up to approximately 670 K, beyond which they decompose into MnTe and  $\text{Bi}_2\text{Te}_3$ . This decomposition affects the material's magnetic properties, requiring adjustments to our results to assess thermoelectric properties at elevated temperatures. For MnTe, a similar approach can be used to determine its thermoelectric properties. Applying pressure increases the stability temperature of these materials. Under pressure, the magnetic properties remain largely unchanged, allowing us to continue using our results [36, 37].

To examine the effects of exchange couplings on the thermoelectric properties, we have investigated the figure of merit of magnetic TIs, where the interaction of magnetic atoms is incorporated into the Ising Hamiltonian with the nearest-neighbor exchange coupling  $J_1$ . In Fig. 10, we have plotted the figure of merit as a func-

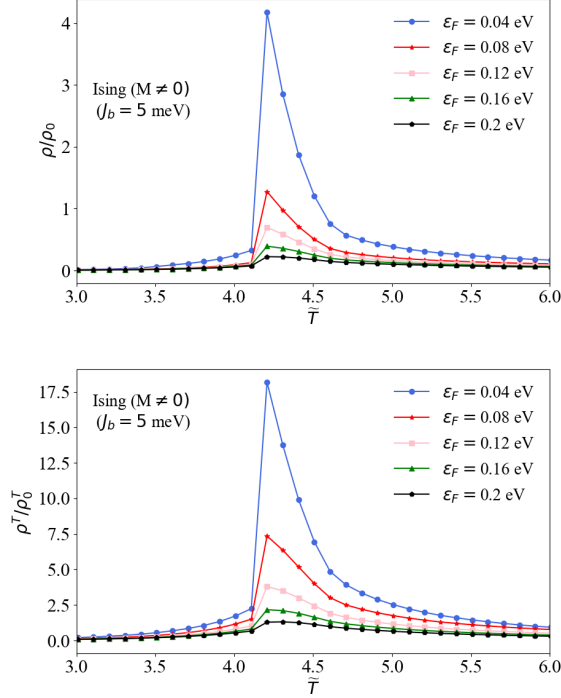


FIG. 11: Transport properties of the surface of the magnetic TI as functions of  $\bar{T} = k_B T / (J_1 \delta^2)$  for various Fermi energy values. The interaction between magnetic atoms on the surface of the TI is governed by the Ising Hamiltonian. Here,  $J_1$  represents the nearest-neighbor exchange coupling, and the ferromagnetic interlayer exchange  $J_c$  is scaled to  $J_1$ , and set to  $+0.18$ . The plots show: electrical resistivity (up) and thermal resistivity (down). The constants  $\rho_0$  and  $\rho_0^T$  are defined in the caption of Figure 8.

tion of  $k_B T / \varepsilon_F$  for different strengths of  $J_1$ . The values considered for exchange coupling are larger than those measured in magnetic TIs, but the observed behavior is also valid for smaller values. As clearly seen, the curve of the figure of merit changes behavior at two temperatures. The first change occurs at the transition temperature, which naturally increases as the exchange coupling increases. The second change is due to the chemical potential becoming zero, which is independent of the exchange coupling values. At much smaller values of the exchange coupling  $J_1$ , the critical temperature shifts to much lower temperatures, and in this case, the changes in the figure of merit at lower temperatures are not noticeable, but eventually, the figure of merit reaches a saturation value of 0.8.

### B. Ising case: Ferromagnetic interlayer interactions

For intrinsic ferromagnetic TIs like  $\text{MnBi}_6\text{Te}_{10}$ , the bulk exhibits temperature-dependent magnetization  $M(T)$ , which in turn induces a temperature-dependent energy gap in the surface electrons. Below the bulk crit-

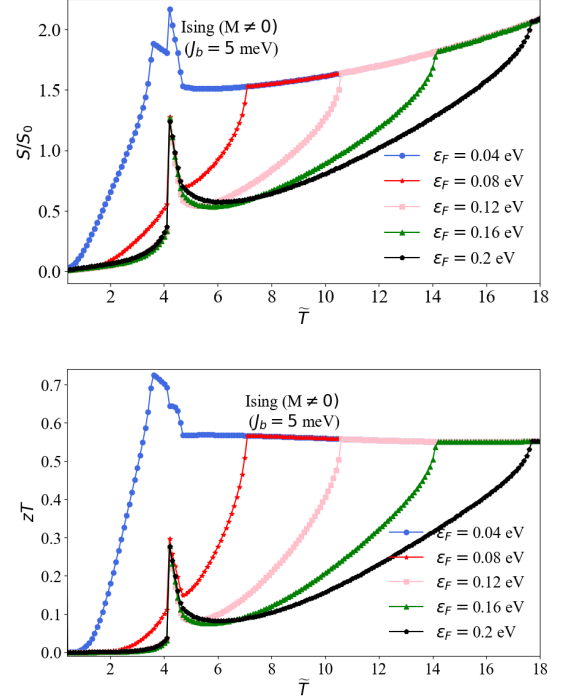


FIG. 12: Thermoelectric properties of the surface of the magnetic TI as functions of temperature. The interaction between magnetic atoms on the surface of the TI is governed by the Ising Hamiltonian. Here,  $J_1$  represents the nearest-neighbor exchange coupling, and the ferromagnetic interlayer exchange  $J_c$  is scaled to  $J_1$ , and set to  $+0.18$ . The plots show: thermopower (up), and thermoelectric figure of merit (down).

ical temperature ( $T < T_c^{\text{bulk}}$ ), the surface states possess a finite energy gap. However, above this critical temperature, the gap closes. This behavior significantly influences the thermoelectric properties of the TI, as detailed below.

The temperature dependence of electrical and thermal resistivities (see Fig. 11), as well as thermopower and the figure of merit (see Fig. 12), are generally similar for both antiferromagnetic and ferromagnetic interlayer interactions. However, there is a subtle difference in thermopower. Below the bulk critical temperature ( $T_c^{\text{bulk}}$ ), the bulk exhibits spontaneous magnetization, leading to the emergence of a surface energy gap. Within this temperature range, significant variations are observed in thermopower and the figure of merit, primarily attributable to the presence of the energy gap, which enhances thermopower below  $T_c^{\text{bulk}}$ . Conversely, above  $T_c^{\text{bulk}}$ , the bulk magnetization vanishes, resulting in thermoelectric properties that closely resemble those of an antiferromagnetic bulk, where the bulk magnetization is inherently zero. This phenomenon occurs because interlayer interactions, besides altering the surface gap, also influence the size and number of clusters. Ferromagnetic interlayer interactions can modify the clusters in a

way that leads to thermopower saturation. It is important to note that the use of an Ising interaction model to describe the bulk magnetization ensures that the surface critical temperature closely aligns with the bulk critical temperature.

### C. Heisenberg interaction between magnetic atoms on the surface of the TI

When the interaction between magnetic atoms on the surface of magnetic TIs is described by the Heisenberg model in Eq. (1), the relaxation time of Dirac electrons is given by Eq. (10). For intrinsic antiferromagnetic TIs, the bulk magnetization  $M$  is zero for all temperatures, resulting in a vanishing surface gap. Consequently,  $\cos \eta_k = 0$ , and the relaxation time simplifies to:

$$\frac{1}{\tau_{k,\theta_s}} = \frac{1}{\tau_0} \bar{n}_{\theta_s} k \xi_{\theta_s} \left( \frac{\xi_{\theta_s}}{a} \right)^3 \frac{2 + \cos^2 \theta_s + 2k^2 \xi_{\theta_s}^2 \sin^2 \theta_s}{(1 + 4k^2 \xi_{\theta_s}^2)^{5/2}}. \quad (15)$$

By utilizing Eq. (15) and numerically solving the integral in Eq. (12), we obtain the electrical and thermal resistivities as functions of temperature, as illustrated in Fig. 13. Overall, their behaviors are remarkably similar to the Ising case, with minor differences. At low temperatures, both electrical and thermal resistivities are nearly zero, regardless of the Fermi energy values. As the temperature increases, unlike the Ising case, there are no tangential changes in the behavior of the resistivities. However, near the critical temperature, they abruptly jump and reach a maximum at the critical temperature  $\tilde{T}_c \simeq 1.42$  ( $T_c \simeq 30$  K). The low-temperature behavior of the resistivities significantly differs from the Ising case due to the different magnetic clustering in the Ising and Heisenberg models. Above the critical temperature, their behaviors are almost the same, and in both cases, resistivities gradually decrease with increasing temperature.

The weak surface resistivity observed in the ferromagnetic phase of the surface pertains only to surface properties. In contrast, the bulk electrical resistivity in the antiferromagnetic (AFM) phase (the magnetic order of the bulk of the antiferromagnetic TI) behaves differently [39, 40]. Experimental evidence shows that in an A-type AFM system, interlayer AFM coupling typically causes strong spin scattering in the ordered state, leading to high resistivity. However, when an external magnetic field is strong enough to overcome this coupling, spin scattering is suppressed, resulting in low resistivity. This phenomenon, known as the spin-valve effect, was first demonstrated in magnetic multilayer thin films. The spin-valve effect can also occur between an A-type AFM and a canted AFM state, as observed in  $\text{Ca}_3\text{Ru}_2\text{O}_7$  and  $\text{MnBi}_2\text{Te}_4$  during magnetotransport measurements [39].

The temperature dependence of thermopower in the Heisenberg case is depicted in Fig. 14. When intra-layer interactions are described by the Heisenberg Hamiltonian, the surface of the topological insulator transitions

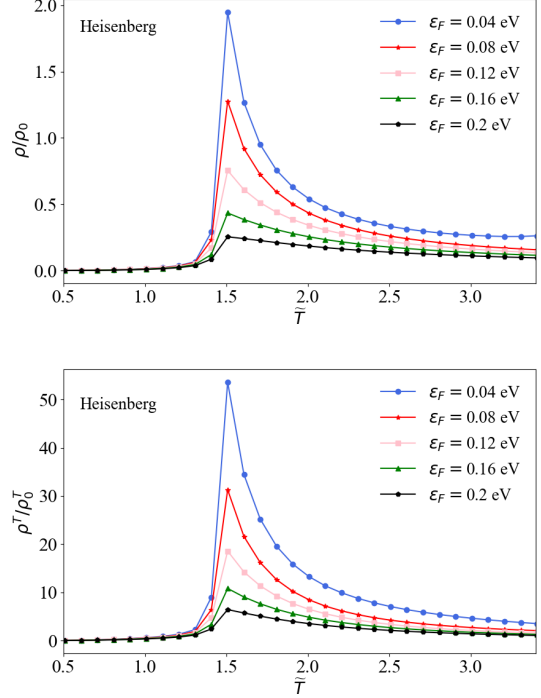


FIG. 13: Transport properties of the surface of the magnetic TI as functions of  $\tilde{T} = k_B T / (J_1 \bar{s}^2)$  for various Fermi energy values. The interaction between magnetic atoms on the surface of the TI is described by the Heisenberg Hamiltonian in Eq. (1). Here,  $J_1$  represents the nearest-neighbor exchange coupling, while  $J_2$ ,  $J_4$ , the uniaxial single ion anisotropy  $D$ , and the antiferromagnetic interlayer exchange  $J_c$  are scaled relative to  $J_1$ , with values set to  $-0.28$ ,  $0.08$ ,  $0.4$ , and  $-0.18$ , respectively. The plots show: electrical resistivity (up) and thermal resistivity (down). The constants  $\rho_0$  and  $\rho_0^T$  are defined in the caption of Figure 8.

to the paramagnetic phase at a significantly lower temperature than observed in the Ising model. As a result, an anomalous increase in thermopower is seen at temperatures above the critical point, even for relatively low values of Fermi energy. At the critical point, the thermopower displays a local peak similar to that in the Ising model; however, this peak is roughly half the magnitude of its Ising counterpart. In the ordered ferromagnetic phase, the thermopower remains very low, while in the disordered phase, it experiences an anomalous jump and increases with temperature. This behavior is largely attributed to magnetic clustering, where, in the paramagnetic phase, the size and number of magnetic clusters are greater than those in the ferromagnetic phase.

We have also illustrated the thermoelectric figure of merit as a function of temperature in Fig. 14. Below the surface critical temperature, the figure of merit approaches zero. At the critical point, it begins to increase with a slight jump, ultimately reaching a saturation value of approximately 0.6 at the temperature where the chemical potential becomes zero. Notably, at lower Fermi ener-

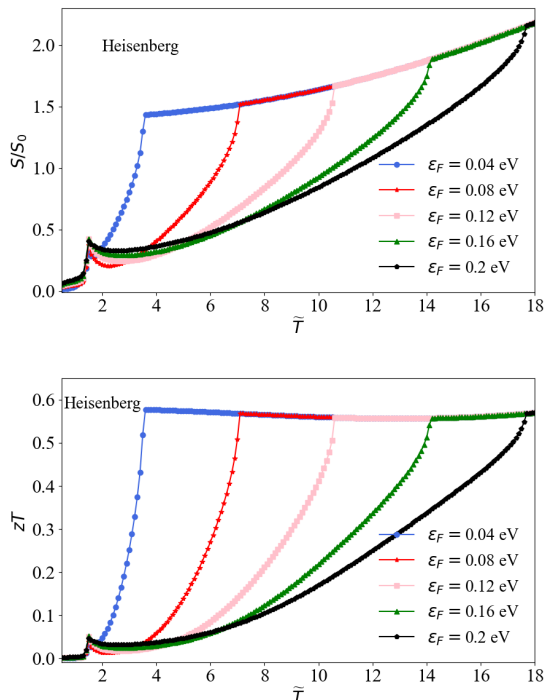


FIG. 14: Thermoelectric properties of the surface of the magnetic TI as functions of temperature  $\tilde{T}$  for various Fermi energy values. The interaction between magnetic atoms on the surface of the TI is described by the Heisenberg Hamiltonian in Eq. (1). Here,  $J_1$  represents the nearest-neighbor exchange coupling, while  $J_2$ ,  $J_4$ , the uniaxial single ion anisotropy  $D$ , and the antiferromagnetic interlayer exchange  $J_c$  are scaled to  $J_1$ , with values set to  $-0.28$ ,  $0.08$ ,  $0.4$ , and  $-0.18$ , respectively. The plots show: thermopower (up), and thermoelectric figure of merit (down). Here, the interlayer interaction is antiferromagnetic and set to  $J_c/J_1 = -0.18$ .

gies, the saturation of the figure of merit occurs at significantly reduced temperatures. For example, with a Fermi energy of 40 meV, the saturation temperature is 230 K. This result is particularly advantageous when compared to other thermoelectric materials that typically operate within mid-temperature ranges of 400 to 900 K [38].

## V. COMPARISON WITH EXPERIMENTS

Extracting the surface resistivity—both electrical and thermal—from experimental data, and disentangling it from bulk contributions, presents substantial methodological challenges. This complexity hampers direct comparison between theoretical predictions and experimental measurements. Aside from specific cases, such as the direct measurement of the surface resistivity of  $\text{Bi}_2\text{Te}_2\text{Se}$  TI in the presence of surface steps [41], the separation of surface and bulk resistivity contributions in magnetic TIs remains largely unresolved in laboratory studies, as confirmed by our literature review. Nonetheless, the surface

resistivity behavior predicted by the magnetic clustering model aligns qualitatively with experimental findings. Notably, the resistivity value derived from the clustering approach—approximately  $3250 \Omega$  at temperatures slightly above the critical temperature (see Fig. 13)—is of the same order of magnitude as the surface resistivity reported in [41] for  $\text{Bi}_2\text{Te}_2\text{Se}$ .

In [42], the authors reported the growth of millimeter-sized  $\text{MnBi}_2\text{Te}_4$  single crystals and observed a drop in electrical resistivity upon cooling across the bulk transition temperature  $T_N$ . They noted critical scattering near  $T_N$  in thermal conductivity, but thermopower showed a linear temperature dependence from 2 K to 300 K without anomalies around  $T_N$ .

In another study [39], the authors systematically measured the variation of resistivity of  $\text{MnBi}_2\text{Te}_4$  in the absence/presence of an external magnetic field. Their results show that the electrical resistivity in  $x$  and  $z$  directions,  $\rho_{xx}(T)$  and  $\rho_{zz}(T)$ , peak at the Neel temperature, and the peaks are suppressed by the magnetic fields higher than a critical value. This observation is consistent with the spin fluctuation-driven spin scattering scenario.

In [40], the electrical transport measurements were carried out on a  $\text{MnBi}_2\text{Te}_4$  single crystal with a thickness of  $\sim 10 \mu\text{m}$ . Their results display the metallic temperature dependence of the longitudinal resistivity  $\rho_{xx}$  from 1.5 K to room temperature. A sharp transition at  $\sim 25\text{K}$  corresponding to the AFM transition is consistent with  $T_N$  from the magnetic property measurement.

In [43], it has been shown that a kink-like transition is observed around the Neel temperature in both the thermopower and electrical resistivity of  $\text{MnBi}_2\text{Te}_4$ . Upon approaching  $T_N$ , spin fluctuations are expected to be stronger, leading to stronger scattering and thus a shorter mean-free-path of electrons and an increase in resistivity. As the long-range magnetic order develops below  $T_N$ , in which spins within the  $x-y$  plane are ferromagnetically aligned, spin fluctuations and the electron-spin scattering are suppressed, resulting in kink in  $\rho$  at  $T_N$  followed by a continuous decrease upon decreasing the temperature. For thermopower, its negative sign over the whole measured temperature range suggests electrons as the dominant charge carriers, which is consistent with the Hall effect transport studies. As the temperature decreases, the entropy per electron decreases, leading to a decrease in thermopower, on the other hand, as will be discussed later, below  $T_N$  the magnon-electron drag effect due to the coherent momentum conserving magnon-electron scattering gives rise to an increase in thermopower. As a result, the net thermopower develops a broad bump around 14 K. The maximum electron contribution below 25 K is  $0.05 \text{ W/mK}$ , much smaller than the increase of thermal conductivity observed below  $T_N$ . Therefore, the main heat carriers in  $\text{MnBi}_2\text{Te}_4$  are phonons and/or magnons. Magnons can contribute to the thermal conduction via two ways. One is that magnons serve as heat carriers, which would lead to an enhanced thermal con-

ductivity below  $T_N$ , the other is that magnons scatter phonons, giving rise to a reduction of the phonon contribution to thermal conductivity. Thus, the increase of thermal conductivity below  $T_N$  indicates the dominance of magnons as heat carriers.

## VI. SUMMARY AND OUTLOOK

Identifying and developing thermoelectric materials capable of converting waste heat into electricity is crucial for advancing clean energy technologies. Among the various materials studied, bismuth telluride and its alloys have received significant attention. This paper theoretically investigates the thermoelectric properties of the surface of magnetic TIs. Our findings demonstrate that the thermopower of the surface of magnetic TIs is comparable to other high-performance thermoelectric materials. The interaction of magnetic atoms on the surface plays a crucial role in achieving high thermopower. Specifically, the exchange interactions between magnetic atoms lead to the formation of magnetic clusters, which scatter Dirac electrons and significantly enhance the thermoelectric properties of the surface.

The results of this study are presented in detail below.

### 1. *Magnetic clustering in Ising and Heisenberg models: A comparative analysis below and above surface critical temperature*

Below the surface critical temperature, the definition of magnetic clusters in the Ising and Heisenberg models is analogous. In the Ising model, spin alignment serves as the criterion for cluster membership. Given that spins in the Ising model assume discrete values of  $+1$  and  $-1$ , this definition is quite effective. However, in the Heisenberg model, spins are vectors with continuous orientations in space, making the alignment criterion less efficient. Therefore, we employ the Wolf probability for magnetic clustering.

Above the critical temperature, within the disordered paramagnetic phase, clustering in the Ising model is based on the energy of links, whereas in the Heisenberg model, the Wolf probability is again utilized. The Wolf probability assigns a greater weight to neighboring spins that are aligned in the same direction. Consequently, on the surface of magnetic TIs with Heisenberg spin interaction, in the paramagnetic phase, short-range ordered ferromagnetic domains are considered magnetic clusters. This approach is not applicable to the Ising model, where spins are restricted to two directions. In the Ising model, spins with the highest link energy with their neighbors are regarded as centers of magnetoresistance generation. For a spin to have the strongest link with its neighbors, it must be aligned with all of them.

We derive our definition of a cluster from GMR experiments. In these experiments, electrons with down spins are scattered by electrons with up spins, while those with up spins pass through without scattering. This concept is discussed in our paper. The initial direction that electrons on the surface of TIs choose is influenced by the initial magnetization, an effect we have implicitly accounted for. Consequently, we define clusters as those that align oppositely to the direction of magnetization. This idea is clearly articulated in the Ising model. However, in the Heisenberg model, where we have various spin directions, we apply the Wolf probability while still maintaining the constraint of opposite alignment to the magnetization.

### 2. *Inaccuracies in thermopower predictions by Mott's relation in magnetic TIs:*

We also computed the thermopower utilizing the Mott' relation [44]. Our findings suggest that the Mott's relation produces unreliable results at temperatures surpassing the critical temperature. In magnetic TIs, the density of surface states demonstrates a linear dependence on energy, which contributes to the discrepancies in predictions made by the Mott relation at temperatures beyond the surface transition temperature. This behavior is analogous to that observed in graphene, where the Mott relation is valid at low temperatures, but significant deviations arise at elevated temperatures due to the linear density of states [45, 46].

### 3. *The violation of the Wiedemann-Franz law in magnetic TIs:*

The Wiedemann-Franz law establishes a relationship between the electrical and thermal resistivities of metals, expressed as  $\rho/\rho^T = LT$ , where  $L$  is the Lorenz number [44, 48]. This law primarily applies to good conductors but is often violated in materials such as topological Kondo model [49], graphene [46], and Weyl-semimetal  $WP_2$  [50].

Materials that adhere to this law typically exhibit a low figure of merit, as they may possess low electrical conductivity. Our findings indicate that for magnetic TIs, the Wiedemann-Franz law holds true only at very low temperatures, similar to the behavior observed in graphene [46]. However, even a slight increase in temperature results in deviations from the law. These deviations stem from the combined effects of spin-orbit interactions on the surfaces of magnetic TIs, the linear energy dependence of the density of states, and the presence of magnetic clusters at temperatures above absolute zero.

### 4. *Validity of Boltzmann transport equation:*

It is important to acknowledge that the Boltzmann transport equation relies on the assumption of weak scattering. However, as we approach the magnetic

critical temperature, scattering becomes strong and potentially non-perturbative, which limits the applicability of the relaxation time approximation at the point where the thermopower peaks. Close to the critical temperature, significant scattering occurs, necessitating the inclusion of additional corrections in the  $s - d$  Hamiltonian. We have partially addressed this through our scattering potential. While we focus on the average cluster size, we can still utilize the Boltzmann transport equation effectively. However, to achieve greater accuracy, it is essential to consider higher-order effects. Here, we have concentrated on the first-order approximation of the Boltzmann transport equation, leaving higher-order approximations for future investigation.

##### 5. *Intrinsic surface gap in MnBi<sub>2</sub>Te<sub>4</sub>*:

Experimental findings on MnBi<sub>2</sub>Te<sub>4</sub> indicate that the nontrivial surface state exhibits a gap of approximately 85 meV, even at temperatures significantly exceeding the Neel temperature [39]. This intrinsic gap in the surface states is likely attributed to strong spin fluctuations within the material. In

this study, we have not considered the impact of the energy gap on the energy spectrum of incident and scattered Dirac electrons. While the presence of a gap does not substantially alter the longitudinal resistivity behavior, it does give rise to phenomena such as skew scattering and the associated anomalous Hall effect.

While we have analyzed the mean-field effects of bulk magnetic atoms on the surface electrons, a more comprehensive approach would involve considering the contributions of magnetic atoms in each layer independently, where the distance of each layer from the surface becomes a critical factor [51].

##### Acknowledgement

We would like to express our gratitude to Prof. D. Vashaee for his valuable comments and insightful discussions. This work is based upon research funded by Iran National Science Foundation (INSF) under project No. 4006266.

- 
- [1] O. Fenwick, and A. Jones, Materials for the Energy Transition roadmap: Materials Thermoelectric Energy Conversion Materials, Henry Royce Institute (2020).
- [2] Chhatrasal Gayner, Kamal K. Kar, Recent advances in thermoelectric materials, Progress in Materials Science **83**, 330 (2016).
- [3] Rakesh Singh, Surya Dogra, Saurav Dixit, Nikolai Ivanovich Vatin, Rajesh Bhardwaj, Ashok K. Sundramoorthy, H.C.S. Perera, Shashikant P. Patole, Rajneesh Kumar Mishra, Sandeep Arya, Advancements in thermoelectric materials for efficient waste heat recovery and renewable energy generation, Hybrid Advances **5**, 100176 (2024).
- [4] Yuri V. Ivanov, Alexander T. Burkov, and Dmitry A. Pshenay-Severin, Thermoelectric Properties of Topological Insulators, Phys. Status Solidi B, 1800020 (2018).
- [5] Y. Zheng, T. Lu, Md M. H. Polash, M. Rasoulianboroujeni, N. Liu, M. E. Manley, Y. Deng, P. J. Sun, X. L. Chen, R. P. Hermann, D. Vashaee, J. P. Heremans, and H. Zhao, Paramagnon drag in high thermoelectric figure of merit Li-doped MnTe, Sci. Adv. **5**, eaat9461 (2019).
- [6] M. M. H. Polash, F. Mohaddes, M. Rasoulianboroujeni, and D. Vashaee, Magnon-drag thermopower in antiferromagnets versus ferromagnets, J. Mater. Chem. C **8**, 4049 (2020).
- [7] M. M. H. Polash, D. Moseley, J. Zhang, R. P. Hermann, and D. Vashaee, Understanding and design of spin-driven thermoelectrics, Cell Rep. Phys. Sci. **2**, 100614 (2021).
- [8] F. Heydarinasab, M. Jazandari, M. M. H. Polash, J. Abouie, and D. Vashaee, Paramagnon heat capacity and anomalous thermopower in anisotropic magnetic systems: Understanding interlayer spin correlations in a magnetically disordered phase, Phys. Rev. B **109**, 054418 (2024).
- [9] N. Xu, Y. Xu, and J. Zhu, Topological insulators for thermoelectrics, npj Quant Mater **2**, 51 (2017).
- [10] Yu Pan, Bin He, Xiaolong Feng, Fan Li, Dong Chen, Ulrich Burkhardt, and Claudia Felser, A magnetothermoelectric with a high figure of merit in topological insulator Bi<sub>88</sub>Sb<sub>12</sub>, Nat. Mater. **24**, 76 (2025).
- [11] Joel E. Moore, The birth of topological insulators, nature **464**, 194 (2010).
- [12] Yoshinori Tokura, Kenji Yasuda, and Atsushi Tsukazaki, Magnetic topological insulators, Nat. Rev. Phys. **1**, 126 (2019).
- [13] K. Vyborny, A. A. Kovalev, J. Sinova, and T. Jungwirth, Semiclassical framework for the calculation of transport anisotropies, Phys. Rev. B **79**, 045427 (2009).
- [14] A. Sabzalipour, J. Abouie, and S. H. Abedinpour, Anisotropic conductivity in magnetic topological insulators, J. Phys.: Condens. Matter **27**, 115301 (2015).
- [15] A. N. Zarezad, and J. Abouie, Transport in magnetically doped topological insulators: Effects of magnetic clusters, Phys. Rev. B **98**, 155413 (2018).
- [16] A. N. Zarezad, and J. Abouie, Transport in two-dimensional Rashba electron systems doped with interacting magnetic impurities, Phys. Rev. B **101**, 115412 (2020).
- [17] K. Akabli, Y. Magnin, Masataka Oko, Isao Harada, and H. T. Diep, Phys. Rev. B **84**, 024428 (2011).
- [18] Pinyuan Wang, Jun Ge, Jiaheng Li, Yanzhao Liu, Yong Xu, Jian Wang, Intrinsic magnetic topological insulators, Innov. **2**, 2-100098 (2021).
- [19] Bing Li, J. -Q. Yan, D. M. Pajerowski, Elijah Gordon, A. -M. Nedic, Y. Sizyuk, Liqin Ke, P. P. Orth, D. Vaknin, and R. J. McQueeney, Competing magnetic interactions

- in the antiferromagnetic topological insulator  $\text{MnBi}_2\text{Te}_4$ , *Phys. Rev. Lett.* **124**, 167204 (2020).
- [20] Bing Li, D. M. Pajerowski, S. X. M. Riberolles, Liqin Ke, J. -Q. Yan, and R. J. McQueeney, Quasi-two-dimensional ferromagnetism and anisotropic interlayer couplings in the magnetic topological insulator  $\text{MnBi}_2\text{Te}_4$ , *Phys. Rev. B* **104**, L220402 (2021).
- [21] A. Fert, and I. A. Campbell, Two-current conduction in nickel, *Phys. Rev. Lett.* **21**, 1190 (1968).
- [22] M. N. Baibich, J. M. Broto, A. Fert, F. Nguyen Van Dau, and F. Petroff, Giant magnetoresistance of (001)Fe/(001)Cr magnetic superlattices, *Phys. Rev. Lett.* **61**, 2472 (1988).
- [23] Alla E. Petrova, E. D. Bauer, Vladimir Krasnorussky, and Sergei M. Stishov, Behavior of the electrical resistivity of MnSi at the ferromagnetic phase transition, *Phys. Rev. B* **74**, 092401 (2006).
- [24] S. M. Stishov, A. E. Petrova, S. Khasanov, G. Kh. Panova, A. A. Shikov, J. C. Lashley, D. Wu, and T. A. Lograsso, Magnetic phase transition in the itinerant helimagnet MnSi: Thermodynamic and transport properties, *Phys. Rev. B* **76**, 052405 (2007).
- [25] Luo Zhi-Huan, Loan Mushtaq, Liu Yan and Lin Jian-Rong, Critical behaviour of the ferromagnetic Ising model on a triangular lattice, *Chinese Phys. B* **18**, 2696 (2009).
- [26] K. Murao, F. Matsubara, and T. Kudo, Anisotropic ferromagnet on a triangular lattice with antiferromagnetic next-nearest-neighbor interactions, *J. Phys. Soc. Jpn.*, **65** 1399 (1996).
- [27] U. Wolff, Lattice field theory as a percolation process, *Phys. Rev. Lett.* **60**, 1461 (1988).
- [28] Coniglio, A and Klein, Clusters and Ising critical droplets: a renormalisation group approach, *Journal of Physics A: Mathematical and General* **13**, 2775 (1980).
- [29] J. Hoshen and R. Kopelman, Percolation and cluster distribution. I. Cluster multiple labeling technique and critical concentration algorithm, *Phys. Rev. B* **14**, 3438 (1976).
- [30] M. M. Otrokov, I. P. Rusinov, M. Blanco-Rey, M. Hoffmann, A. Yu. Vyazovskaya, S. V. Ereemeev, A. Ernst, P. M. Echenique, A. Arnau, E. V. Chulkov, Unique thickness-dependent properties of the van der Waals interlayer antiferromagnet  $\text{MnBi}_2\text{Te}_4$  films, *Phys. Rev. Lett.* **122**, 107202 (2019).
- [31] Yi-Fan Zhao, Ling-Jie Zhou, Fei Wang, Guang Wang, Tiancheng Song, Dmitry Ovchinnikov, Hemian Yi, Ruobing Mei, Ke Wang, Moses H W Chan, Chao-Xing Liu, Xiaodong Xu, Cui-Zu Chang, Even-Odd layer-dependent anomalous Hall effect in topological magnet  $\text{MnBi}_2\text{Te}_4$  thin films, *Nano. Lett.* **21**, 7691 (2021).
- [32] Jifeng Shao, Yuntian Liu, Meng Zeng, Jingyuan Li, Xuefeng Wu, Xiao-Ming Ma, Feng Jin, Ruie Lu, Yichen Sun, Mingqiang Gu, Kedong Wang, Wenbin Wu, Liusuo Wu, Chang Liu, Qihang Liu, and Yue Zhao, Pressure-tuned intralayer exchange in superlattice-like  $\text{MnBi}_2\text{Te}_4/(\text{Bi}_2\text{Te}_3)_n$  topological insulators, *Nano Lett.* **21**, 5874 (2021).
- [33] Padmanabhan H, Stoica VA, Kim PK, Poore M, Yang T, Shen X, Reid AH, Lin MF, Park S, Yang J, Wang HH, Koocher NZ, Puggioni D, Georgescu AB, Min L, Lee SH, Mao Z, Rondinelli JM, Lindenberg AM, Chen LQ, Wang X, Averitt RD, Freeland JW, Gopalan V., Large Exchange Coupling Between Localized Spins and Topological Bands in  $\text{MnBi}_2\text{Te}_4$ , *Adv Mater.* **49**, e2202841 (2022).
- [34] Dong Sun Lee, Tae-Hoon Kim, Cheol-Hee Park, Chan-Yeup Chung, Young Soo Lim, Won-Seon Seoa and Hyung-Ho Park, Crystal structure, properties and nanostructuring of a new layered chalcogenide semiconductor,  $\text{MnBi}_2\text{Te}_4$ , *Cryst. Eng. Comm.* **15**, 5532–5538 (2013).
- [35] Yun Zheng, Xian Yi Tan, Xiaojuan Wan, Xin Cheng, Zhihong Liu, Qingyu Yan, Thermal stability and mechanical response of  $\text{Bi}_2\text{Te}_3$ -based materials for thermoelectric applications, *Applied Energy Materials* **3**, 2078 (2020).
- [36] Le Fang, Chen Chen, Xionggang Lu, and Wei Ren, Effects of pressure and temperature on topological electronic materials  $\text{X}_2\text{Y}_3$  ( $\text{X} = \text{As, Sb, Bi}$ ;  $\text{Y} = \text{Se, Te}$ ) using first-principles, *Phys. Chem. Chem. Phys.* **25**, 20969 (2023).
- [37] Jonas Anversa, Sudip Chakraborty, Paulo Piquini, and Rajeev Ahuja, High pressure driven superconducting critical temperature tuning in  $\text{Sb}_2\text{Se}_3$  topological insulator, *Appl. Phys. Lett.* **108**, 212601 (2016).
- [38] Zhenglong Tang, Lipeng Hu, Tiejun Zhu, Xiaohua Liu, and Xinbing Zhao, High performance *n*-type Bismuth Telluride based alloys for mid-temperature power generation, *J. Mater. Chem. C* **3**, 10597 (2015).
- [39] Seng Huat Lee, Yanglin Zhu, Yu Wang, Leixin Miao, Timothy Pillsbury, Hemian Yi, Susan Kempinger, Jin Hu, Colin A. Heikes, P. Quarterman, William Ratcliff, Julie A. Borchers, Heda Zhang, Xianglin Ke, David Graf, Nasim Alem, Cui-Zu Chang, Nitin Samarth, and Zhiqiang Mao, Spin scattering and noncollinear spin structure-induced intrinsic anomalous Hall effect in antiferromagnetic topological insulator  $\text{MnBi}_2\text{Te}_4$ , *Phys. Rev. Research* **1**, 012011(R) (2019).
- [40] Hao Li, Shengsheng Liu, Chang Liu, Jinsong Zhang, Yong Xu, Rong Yu, Yang Wu, Yuegang Zhang, and Shoushan Fan, Antiferromagnetic topological insulator  $\text{MnBi}_2\text{Te}_4$ : synthesis and magnetic properties, *Phys. Chem. Chem. Phys.* **22**, 556 (2020).
- [41] Wonhee Ko, Saban Hus, Hoil Kim, Jun Sung Kim, Xiao-Guang Zhang, and An-Ping Li, Resistivity of Surface Steps in Bulk-Insulating Topological Insulators, *Front. Mater.* **9**, 887484 (2022)
- [42] J.-Q. Yan, Q. Zhang, T. Heitmann, Zengle Huang, K. Y. Chen, J.-G. Cheng, Weida Wu, D. Vaknin, B. C. Sales, and R. J. McQueeney, Crystal growth and magnetic structure of  $\text{MnBi}_2\text{Te}_4$ , *Phys. Rev. Materials* **3**, 064202 (2019).
- [43] H. Zhang, C. Q. Xu, S. H. Lee, Z. Q. Mao, and X. Ke, Thermal and thermoelectric properties of an antiferromagnetic topological insulator  $\text{MnBi}_2\text{Te}_4$ , *Phys. Rev. B* **105**, 184411 (2022).
- [44] M. Jonson, and G. D. Mahan, Mott's formula for the thermopower and the Wiedemann-Franz law, *Phys. Rev. B* **21**, 4223 (1980).
- [45] Tomas Löfwander and Mikael Fogelström, Impurity scattering and Mott's formula in graphene, *Phys. Rev. B* **76**, 193401 (2007).
- [46] P. Ray, K. Sarkar, Mott and Wiedemann Franz Law for Monolayer Graphene for Different Scattering Mechanisms. In: Mishra, Y.K., Lingamallu, G., Ghosh, T. (eds) Selected Articles from the 2nd International Conference on Advanced Nanomaterials and Applications. ICANA 2024. Springer Proceedings in Physics, vol 413. Springer, Singapore, (2025).

- [47] M. A. Manyá , G. B. Martins, and M. S. Figueira, Spin-orbit coupling effects on thermoelectric transport properties in quantum dots, *Phys. Rev. B* **105**, 165421 (2022).
- [48] A. Grunwald and J. Hajdu, Note on the Wiedemann-Franz law and the Mott rule in two-dimensional systems in strong magnetic fields, *Z. Phys. B Condensed Matter* **60**, 235 (1985).
- [49] Francesco Buccheri, Andrea Nava, Reinhold Egger, Pasquale Sodano, and Domenico Giuliano, Violation of the Wiedemann-Franz law in the topological Kondo model, *Phys. Rev. B* **105**, L081403 (2022).
- [50] Alexandre Jaoui, Benoit Fauque, Carl Willem Rischau, Alaska Subedi, Chenguang Fu, Johannes Gooth, Nitesh Kumar, Vicky Süß, Dmitrii L. Maslov, Claudia Felser, and Kamran Behnia, Departure from the Wiedemann–Franz law in WP2 driven by mismatch in T-square resistivity prefactors, *npj Quant Mater* **3**, 64 (2018).
- [51] Hai-Peng Sun, C. M. Wang, Song-Bo Zhang, Rui Chen, Yue Zhao, Chang Liu, Qihang Liu, Chaoyu Chen, Hai-Zhou Lu, and X. C. Xie, Analytical solution for the surface states of the antiferromagnetic topological insulator  $\text{MnBi}_2\text{Te}_4$ , *Phys. Rev. B* **102**, 241406(R) (2020).